ChemComm

FEATURE ARTICLE

View Article Online
View Journal | View Issue

Cite this: *Chem. Commun.*, 2026, **62**, 9773

Chemistry in evaporating sessile droplets

Sujay Paul [a] and Arun Chattopadhyay *[ab]

Sessile droplet evaporation is a fundamental natural process that plays an important role in inkjet printing-based two-dimensional (2D) thin-film fabrication. The deposit kinetics and the nature of the deposition of microparticles are well-known; however, studies on nanoparticle-laden droplet evaporation have only recently been reported by our laboratory. The unique chemical phenomena associated with evaporating droplets need special attention in order to harness the potential of their applications. Apart from the physical phenomena of fluid dynamics and nanoparticle movement, understanding the chemistry on the surface of nanoparticles and chemical interactions between nanoparticles and solvent in the deposits is of great importance. In our investigations, we have used surface-enhanced Raman spectroscopy to monitor the deposition of chemically functionalized nanoparticles, chemical interactions, and reactions on the surface of deposited nanoparticles at the three-phase contact line. This review highlights the discovery of single-phase transitions in the deposition of plasmonic nanoparticles of different sizes and initial concentrations, as opposed to the well-known gradual deposition of microparticles. Importantly, the study led to the distinction between intrananoparticle and internanoparticle plasmon-catalyzed reactions. The effect of the pH of the medium on the transition from single to multiple steps of deposition of nanoparticles and their distribution across the annulus of the ring deposit constitutes important observations in this regard. A salient feature is the observation of anomalous 2D crystal formation upon evaporation of droplets of molecular solutions. Finally, this article concludes by discussing the potential of the newly discovered chemistry of nanoparticle deposition for future research in liquid-based printing and 2D moiré superlattices.

Received 23rd February 2026,
Accepted 8th April 2026

DOI: 10.1039/d6cc01128d

rsc.li/chemcomm

[a] *Department of Chemistry, Indian Institute of Technology Guwahati, Guwahati 781039, Assam, India. E-mail: arun@iitg.ac.in, sujaypaul@iitg.ac.in*
[b] *Centre for Nanotechnology, Indian Institute of Technology Guwahati, Guwahati – 781039, Assam, India*

Sujay Paul

Sujay Paul obtained his BSc (Hons) degree in Chemistry from the University of Kalyani, India, in 2016 and an MSc degree in Chemistry from the Indian Institute of Technology Guwahati, India, in 2018. He was a CSIR Research Fellow and received his PhD degree in Chemistry from the Indian Institute of Technology Guwahati in 2025, under the supervision of Prof. Arun Chattopadhyay. His research area includes the discovery of novel phenomena in evaporating droplets by normal Raman and surface-enhanced Raman spectroscopic measurements. He is currently pursuing his research career as a Senior Research Fellow (SRF) at the Centre for Nanotechnology, IIT Guwahati.

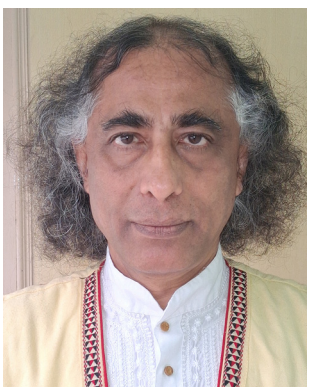

Arun Chattopadhyay

Arun Chattopadhyay is a Professor of Chemistry and is also associated with the Centre for Nanotechnology at IIT Guwahati, India. He received his PhD in Chemical Physics from Columbia University in 1992 and then pursued his postdoctoral research at Stanford University (1992–1995). His laboratory has been working on the programmed assembly of nanoscale particles, such as atomic clusters, metal nanoparticles, quantum dots, and carbon dots. Using Raman spectroscopy, his student and he recently discovered novel chemistry in evaporating sessile droplets. His laboratory is currently developing a new field on the solution-phase synthesis of molecular moiré superlattices and is also pursuing their application potential as quantum matter.

1. Introduction

Pursuing the chemistry of evaporating sessile droplets assumes significance in the wake of current advancements in manufacturing sensors, catalysts, and biomedical devices by the utilization of inkjet printing at various length scales.[1–3] While the chemistry in microdroplets is currently a scientific focus, especially in catalysis-free chemical reactions, studies on the chemistry occurring in evaporating droplets have yet to gain momentum. A sessile droplet is more than a system of evaporating solvent and depositing particle: it is a sophisticated non-equilibrium process that can provide a high order of temporal and spatial control for the assembly of nanoscale particles and molecules.[4–6] Moreover, sessile droplets can concentrate solutes, drive local parameter gradients (such as concentration), and direct nanoparticle assembly and orientation through evaporation.[7] Therefore, an evaporating sessile droplet can act as a 'chemical micro-laboratory' that allows precise monitoring of novel physical and chemical processes that are difficult to observe in the bulk liquid or solid state. Beyond the common air–liquid or solid–liquid interfaces, the characteristics of droplets within the surrounding fluid or complex colloids also represent areas of significant growth in industrial techniques and biomedical engineering. For example, the presence of external fluid introduces an extra degree of freedom, which has been useful for 'breath-figure'-driven templating on evaporating polymer solution,[8] enhanced oil recovery by manipulating droplets,[9] and targeted drug delivery using fat drops through the bloodstream.[10] Thus, advanced research in the field is of significance because the deposition kinetics and the structure of the deposited nanoscale particles or molecules (in the form of a ring, popularly known as the ''coffee ring'') determine the application potential of the deposited entities. Controlling the nature of the deposited structure is also important for maximizing the application potential.

Evaporation-induced particle deposition is a complex and fascinating phenomenon that bridges colloid science, fluid dynamics, and surface and interface chemistry. This apparently basic action is present in many natural processes, such as mineral and salt deposits, dew and leaf patterns, and biofilm formation, in industrial applications, such as in the inkjet printing of electronics, flexible devices and wearables, and in healthcare applications, such as printing of artificial cartilage, skins and cellular structure.[11–18] The particle or solid deposition during the evaporation of the solvent is strongly dependent on particle size and shape, the nature of the solvent, the morphology of the substrate, and temperature and humidity conditions, which can drastically alter the deposition pattern and dynamics.[19–23] Advances in experimental methods using optical microscopy have enhanced our understanding of particle motion, dynamics, and deposition.[24] For example, horizontal advective motion of micron-sized particles during the formation of the 'coffee ring' was revealed by fluorescence microscopy and videography.[25] During the evaporation of the solvent, the physical state of the particles inside a sessile droplet changes from the dispersion phase to deposited phase. It has also been found that the microparticles are transported from the bulk phase to the pinned three-phase contact line (TPCL) due to enhanced evaporation of the solvent there.[25] The transportation and deposition occur linearly with time, accompanied by a sudden jump at the final leg of drying.[25,26] The end result is the ''coffee ring'' deposit.

On the other hand, such detailed examinations are important for nanoparticle and molecular systems, owing to their impact on applications such as biomolecular sensing, high-resolution device fabrication, and solid-state plasmon catalysis.[27–29] Nanoparticles are often functionalized with small molecules serving as ligands to improve their stability in the dispersion medium, for organization into higher-order structures, and for practical applications.[30,31] The chemical nature of the ligand-stabilized particles is key to their organization into higher-order hierarchical structures and for functions such as molecular recognition and sensing. Weak intermolecular forces, such as electrostatic and van der Waals interactions, and weak chemical forces, such as hydrogen bonding, play important roles in the aforementioned functions.[32] By altering the surface chemistry of the particles, for example, through the incorporation of reactive functional groups, the interactions between the particles can be modulated, which may result in novel forms of deposition.[33]

When the depositing nanoparticles carry reactive functionalized molecules, the formation of chemical bonds between the molecules on a nanoparticle surface or between two or more nanoparticles results in altered deposition characteristics. Furthermore, the chemical reactions on the surface of depositing nanoparticles before, during, and following deposition may significantly influence the overall deposition mechanism. Moreover, the deposition mechanism may vary depending on the location at the TPCL; for example, depositions at the outer, middle, and inner boundary of the ring could differ with respect to their times as well as the nature of deposition. Therefore, a deeper chemical understanding is necessary to effectively modulate the evaporation-induced nanoparticle deposition. Surface chemistry at the molecular level, such as chemical interactions between the molecules on the particles, interaction between the solvent and the surface of the particles and chemistry of the solvent, are also key factors that influence the deposition mechanism.

Metal nanoparticles have the unique ability to host the localized surface plasmon.[34] The presence of resonant external electromagnetic radiation of appropriate frequency results in an enhancement of the local electric field in the vicinity of an individual nanoparticle, which is referred to as localized surface plasmon resonance (LSPR).[34] In addition, plasmonic 'hot spots', with a higher localized electric field, are generated at the interface of two adjoining nanoparticles.[35] This amplified field in the agglomerated or solid state boosts the photocatalytic efficiency and significantly enhances Raman scattering.[29] In the dispersion phase, the particles are far from each other, and, thus, Raman scattering efficiency remains low, usually preventing meaningful measurement results. On the other hand, when the nanoparticles are deposited on a substrate surface, plasmonic 'hot-spots' are generated that significantly

enhance the scattering efficiency. Therefore, surface-enhanced Raman spectroscopy (SERS) can be utilized to monitor nanoparticle deposition kinetics at the TPCL.[36] Moreover, chemical interactions on the surface of the nanoparticles can also be monitored from the vibrational Raman signals of the functional groups of the ligands stabilizing the nanoparticles.[37]

An important question that is relevant here is to ask about the nature and mechanism of depositions when droplets containing molecular solutions are evaporated. Evaporation of a molecular solution often produces crystalline materials. It has recently been reported that molecular crystals can also generate surface plasmon effects and, thus, could be probed by Raman spectroscopy.[38,39] Therefore, the evaporation-induced solidification of molecules through deposition at the TPCL could be probed using SERS, and a more in-depth understanding of such depositions could be achieved. This is an open field that needs attention and may bring new opportunities in understanding molecular assembly formation, such as crystallization. Pursuing such investigations could be considered important from the standpoint of both fundamental science and technology.

This feature article introduces the recent discovery of a novel deposition mechanism of surface-functionalized nanoparticles, through a single-phase transition at the TPCL, as probed by SERS.[40] The functional groups of the molecules act as stabilizing agents for the nanoparticles in the dispersion and also as chemical probes, giving rise to a significant Raman signal intensity when the nanoparticles are deposited on the substrate surface.[40] This has led to the discovery of a new chemistry in the form of distinctions between intrananoparticle and internanoparticle plasmon-catalyzed reactions, which is also reported herein.[41] Interestingly, the deposition characteristics are strongly dependent on the initial pH of the nanoparticle dispersion; thus, the photochemical reaction in the medium and in the deposits led to a competition between them, resulting in multiple steps of deposition and chemical reactions.[42] In addition, the article highlights the observations of anomalous 2D crystalline depositions of molecules following evaporation of droplets of their solutions.[43] Raman spectroscopic measurements also revealed different vibrational features of molecules on the surface and interior of the 2D crystals, which were further extended to 3D crystals in order to unravel the generality of the differences between surface molecular vibrations and those in the interior of molecular crystals.[43]

2. An overview of evaporation-induced micron-sized particle deposition

Evaporation of droplets is a general method to concentrate dispersed particles into a desired deposition pattern. A common pattern formed by this process is the ''coffee-ring'', where dispersed particles are preferentially deposited at the edge of the droplet, forming a ring-like stain, as shown in Fig. 1. Earlier experiments on droplets were focused on the discovery of solvent evaporation rate and solvent diffusion models. The droplet can evaporate through a constant contact angle mode (with decreasing contact radius) or a constant contact radius mode (with decreasing contact angle).[44,45] It has been reported that the evaporating sessile droplet is always in a thermodynamic non-equilibrium condition with the air, and the slightly higher vapor pressure on the surface of the droplet than in the surrounding atmosphere drives the droplet to evaporate.[46] The inhomogeneous evaporation of the solvent from the surface of a droplet is crucial for the movement of particles inside the droplet. Geometrical and mathematical models for the evaporation of solvent on a solid surface had also been proposed.[47,48] Later, the enhanced evaporation flux at the TPCL was explained experimentally and theoretically.[49] For a droplet pinned on a substrate surface, the enhanced evaporation of the solvent at the TPCL drives advective migration of the particles from the center towards the contact line. Experimental evidence obtained by Deegan, based on fluorescence microscopy measurements and theoretical modeling, established that the number

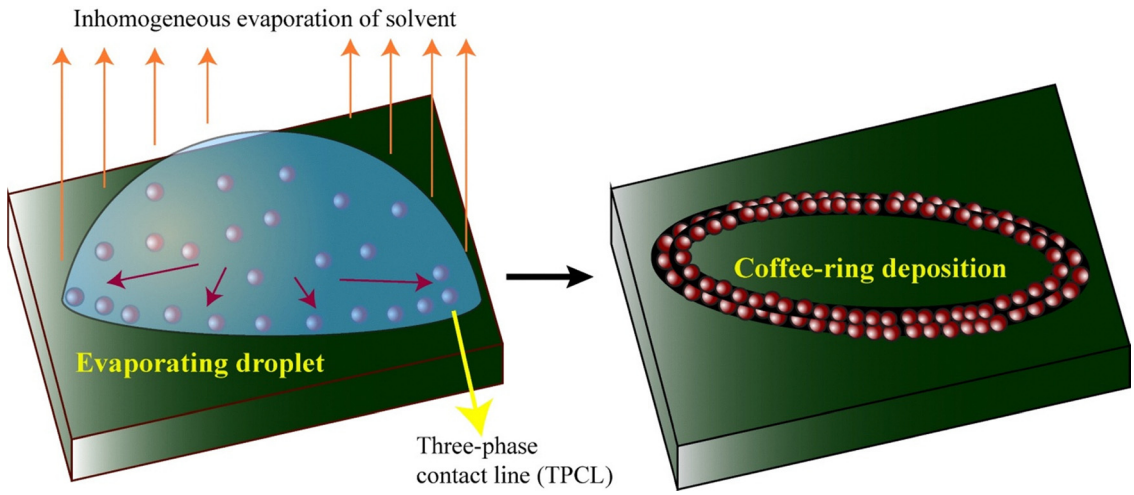

Fig. 1 Schematic of the evaporation-induced ''coffee-ring'' deposition of micron-sized particles at the three-phase contact line of a droplet.

of particles deposited at the contact line increases linearly with time, with accelerated deposition in the final leg of the drying of the droplet.[25] Similar linear deposition of microparticles in wet environments was found by Boulogne and coworkers.[26] In general, the particles are deposited uniformly across the annulus of the ring.

2.1. Effect of substrate on solvent evaporation and particle deposition

The droplet evaporation process is affected by a complex combination of surface chemistry, fluid dynamics and heat transfer. The evaporation rate of the solvent differs significantly and becomes more complex when the liquid is placed on a solid surface, as shown in Fig. 1, compared to that when a fully spherical droplet is in free space. It has been found that a fully spherical droplet having contact angle of 180° on a substrate evaporates slower than the free-standing spherical drop because of the presence of solid surface which hinders the evaporation from below the droplet.[50] It has also been reported that the rate of evaporation of solvent is faster on a hydrophilic substrate than on a hydrophobic surface.[51] Moreover, substrate roughness plays a crucial role in the wetting hysteresis and the evaporation time.[51] Surface roughness also determines the deposited pattern and droplet pinning. With increasing substrate roughness, the contact angle decreases, and the effective contact area between the substrate and droplet increases.[52] This leads to an increase in the evaporation rate of the solvent and a strong capillary flow, making a perfect coffee-ring deposition. This is why we used a commercially available hydrophilic glass substrate in all our experiments described below.

3. Discovery of a phase-transition driven deposition of nanoparticles

Our laboratory recently discovered that nanoparticles dispersed in an evaporating sessile droplet are deposited at the TPCL through a single transition from dispersion to the deposit phase.[40] The thermal stability of the substrate and its surroundings is important because the cooling effect on the droplet surface is dependent on the thermal properties of the substrate.[53] It was also found that, upon decreasing the surrounding atmospheric pressure, the droplet evaporation rate increased.[54] Hence, before carrying out the evaporation-induced nanoparticle deposition experiments, the temperature and humidity of the surrounding environment were kept constant in an air-conditioned room. The mechanism of deposition was pursued using SERS with sodium 4-mercaptobenzoate (NaMBA) as the chemical probe, which functionalized plasmonic gold nanoparticles (AuNPs) in aqueous dispersions. Before the coffee-ring formation experiment, the AuNPs were functionalized with NaMBA. The MBA ions easily attached to the surface of the AuNPs through the formation of strong Au–S bonds.[55] We observed coffee-ring formation of NaMBA attached AuNPs (NaMBA@AuNPs) under ambient conditions at the TPCL. Studies on the kinetics of concentration- and size-dependent particle deposition, and consequent chemical changes surrounding the deposited nanoparticles, revealed novel phenomena that were fundamentally different from the mechanism of micron-sized particle deposition. In a similar vein, deposition of molecular crystals from droplets of their solutions was investigated. The experimental setup that was used is presented schematically in Fig. 2.

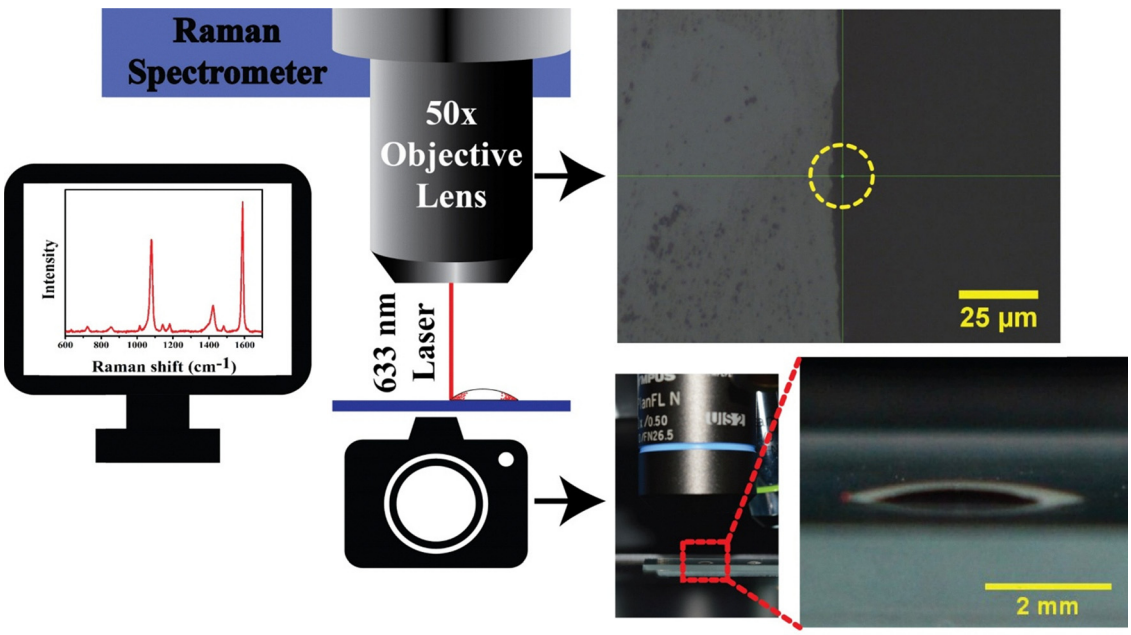

Fig. 2 Schematic of the experimental setup for measuring the coffee-ring formation and related Raman scattering. Reproduced with permission from ref. 40; Copyright 2023, the American Chemical Society.

The Raman scattering peak at 1078 cm^{-1}, which represents a combination of C=C aromatic ring breathing and C–S stretching vibrations, was selected to monitor the deposition of the nanoparticles at the TPCL.[56] In particular, changes in the intensity of the peak over time were used to quantify the measurements. During the initial 25 min of evaporation, the Raman signal intensity was negligible (Fig. 3B). Thus, the signal due to the dispersed particles was absent, making it easier to follow the depositions. Although droplet height and contact angle decreased linearly with time (Fig. 3A), a significant increase in peak intensity occurred at 27.5 min (Fig. 3B), reaching a maximum at 30 min (Fig. 3C), which was followed by a gradual decrease until 42.5 min. The signal then dropped sharply when the droplet fully evaporated at 45.0 min. Such behavior was typical of dispersions containing spherical particles of a particular size when the droplets were evaporated on a glass slide under identical experimental conditions.

Initially, as the droplet evaporates, particles are transported to the TPCL by capillary flow. This would theoretically lead to a steady, monotonous increase in particle concentration at the TPCL. Consequently, a continuous rise in signal intensity or linear deposition of particles could be observed. Solid deposition not only increases the particle concentration but also makes plasmonic 'hot-spots' around the nanoparticles in aggregates.[29] These 'hot spots' greatly amplify the Raman signal, explaining the significant increase in intensity observed in a short time window that is commensurate with the transition from a liquid dispersion to a solid deposit. Therefore, the deposition of nanoparticles at the TPCL follows a 'phase transition', which is fundamentally different from the microparticle deposition mechanism.

Importantly, the drop in the signal intensity following the phase transition is linked to the loss of water, as water is a superior dielectric for SERS compared to air.[57] To confirm this, a separate experiment was conducted in which water was added back to the dried ring at the same spot on the TPCL. As shown in Fig. 3D, the signal intensities returned to their original high values upon rehydration and then decreased again after the water evaporated. The experiment confirmed that the presence of water directly influences the SERS signal intensity, and the loss of signal following drying of the droplet was due to the loss of water surrounding the nanoparticles.

3.1. Nanoparticle concentration- and size-dependent deposition kinetics

It is reported that, in a mixture of two different-sized particles, the solid at the outermost boundary of the ring deposit mainly consists of smaller particles.[58] This technique is utilized to separate particles of different sizes through the formation of coffee rings.[58] In addition, dispersed particle concentration and ambient humidity are known to affect the microparticle deposition kinetics and patterns.[19,23] Our recent results using

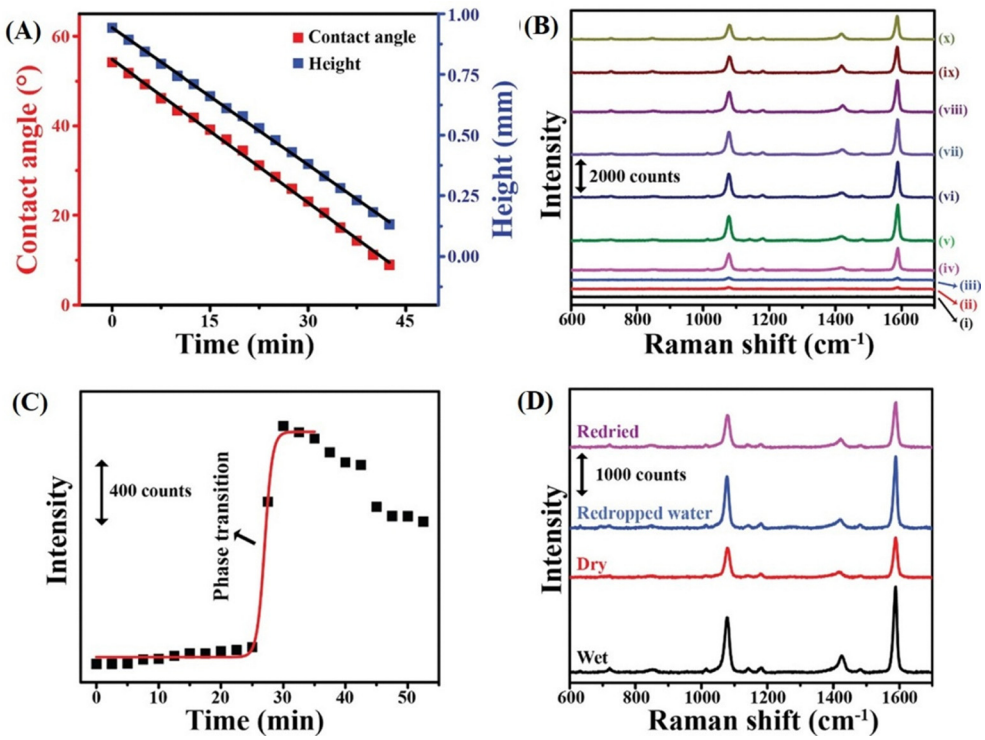

Fig. 3 (A) Plot of variation in the contact angle and droplet height with time. Black lines are linear fits. (B) Raman spectra of an evaporating droplet containing NaMBA-AuNP-2 at a fixed spot on the three-phase contact line recorded at different times. (C) Plot of the intensity of the 1078 cm^{-1} Raman peak *vs.* time, with the Boltzmann fitting of sigmoidal growth shown as a red curve. (D) SERS spectra of NaMBA-AuNP-2 in wet and dry conditions and after subsequent addition of water and redrying. The spectra were recorded at the same spot of a coffee ring. Reproduced with permission from ref. 40; Copyright 2023, the American Chemical Society.

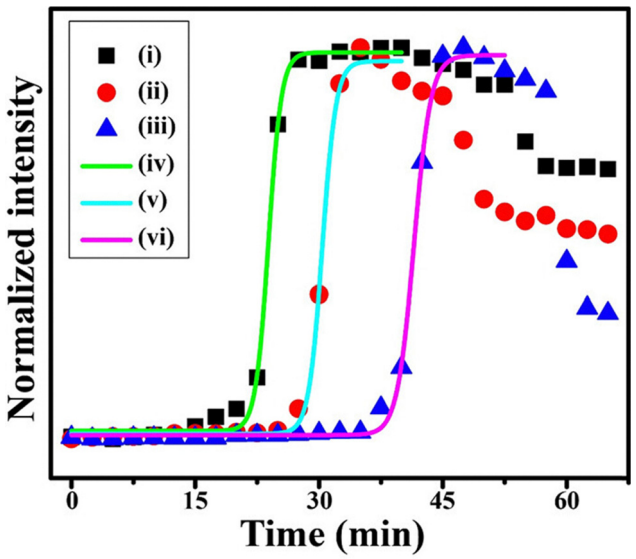

Fig. 4 Time-dependent intensity variation of the 1078 cm^{-1} Raman peak of evaporating droplets containing AuNPs at (i) 10 nM, (ii) 2.5 nM, and (iii) 1.25 nM initial concentrations and the corresponding fitted curves marking the phase transition regions, (iv), (v), and (vi), respectively. Reproduced with permission from ref. 40; Copyright 2023, the American Chemical Society.

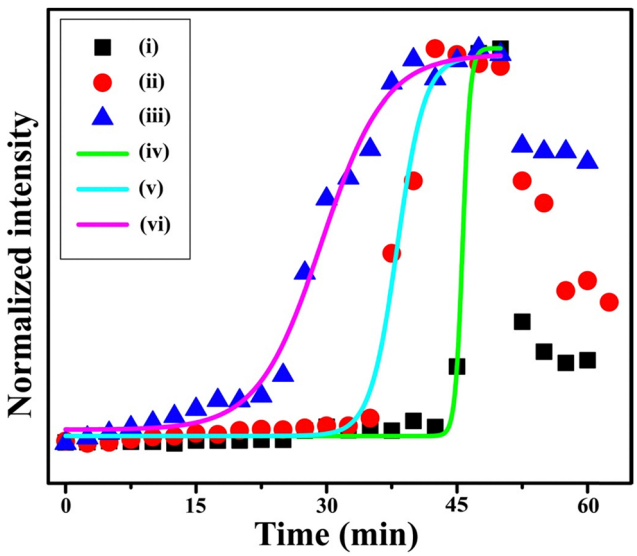

Fig. 5 Time-dependent intensity variation of the 1078 cm^{-1} Raman peak of evaporating droplets, each containing 5 nM of NaMBA-capped (i) 15.4 nm AuNPs, (ii) 25.3 nm AuNPs, and (iii) 36.4 nm AuNPs and the corresponding Boltzmann fitted curves marking the phase transition regions (iv), (v) and (vi), respectively. Reproduced with permission from ref. 40; Copyright 2023, the American Chemical Society.

the chemical probe on the surface of AuNPs of different concentrations and sizes revealed novel results about the deposition kinetics. Experiments were conducted using 25 nm AuNPs (AuNP-2) at initial concentrations of 10 nM, 2.5 nM and 1.25 nM. The time-dependent Raman signal intensities at 1078 cm^{-1} for the three different initial AuNP concentrations are shown in Fig. 4. The times at which the maximum intensity and hence the phase transition occurred were 24.0 min, 32.9 min, and 41.5 min for the 10 nM, 2.5 nM, and 1.25 nM concentrations, respectively. Using initial AuNP concentrations of 10 nM, 2.5 nM, and 1.25 nM, we calculated the phase transition concentrations to be 11.18 ± 2.86 μM, 12.23 ± 0.27 μM, and 15.37 ± 3.52 μM, respectively. The average phase transition concentration for the 25 nm AuNP was determined to be 12.93 ± 3.17 μM, representing the transition from the dispersed to the solid phase.

The surface or liquid–air interface of a sessile droplet usually tends to flatten into an ellipsoid shape due to gravity. The mathematical model of ellipsoidal-cap geometry, considering droplet base radius, contact angle, and height, has been invoked to explain the solvent evaporation rate, change in drop volume, and surface area with time.[59] In our evaporation-induced coffee-ring formation experiments (mentioned in ref. 40 and in this section), the radii of the sessile droplets were maintained below the capillary length of the water droplet, such that the effect of gravity was negligible. Moreover, according to the reported results, a small droplet with a contact angle of less than 90° evaporates in constant contact radius mode and maintains its spherical cap shape.[60] Although the proposed ellipsoidal model is more accurate, we utilized the spherically capped droplet model given in ref. 40 to calculate the volume of the TPCL region where NPs were depositing.

During droplet evaporation, the phase-transition time at the TPCL varied with the size of the AuNPs. For 15.4 nm (AuNP-1) particles, the phase transition occurred at 45.7 min, while for 25.3 nm (AuNP-2) and 36.4 nm (AuNP-3) particles, the phase transition times were at 38.2 min and 29.4 min, respectively (Fig. 5). The difference in phase transition times for different particle sizes can be attributed to two main factors: (i) particle size-dependent diffusion behavior and (ii) packing fraction in the solid deposit. Consequently, smaller particles diffuse more strongly.[61] During evaporation, faster diffusion increases the time required for smaller nanoparticles to accumulate at the TPCL and reach the required critical concentration for deposition. The packing fraction of spherical particles decreases as the diameter increases.[62] Fewer large particles are needed to reach a certain packing fraction and transition from the dispersed medium to the solid deposit. Because of this, the largest AuNPs reached the critical concentration for phase transition much sooner than the medium-sized AuNPs, which, in turn, deposited earlier than the smallest AuNPs. We observed the concentrations required for the phase transition of 15.4 nm AuNPs to be 146.10 ± 20.99 μM and for 36.4 nm AuNPs to be 3.21 ± 0.12 μM. The experiment with the 25.3 nm AuNPs showed a phase-transition concentration of 14.84 ± 1.33 μM, which matches our findings mentioned in the previous section.

4. Distinction between intrananoparticle and internanoparticle plasmon-catalyzed reactions

In chemistry, intramolecular and intermolecular reactions differ in their kinetics, dynamics, and product selectivity, often

influenced by stereochemistry.[63–67] Understanding these differences has been crucial for developing multi-step industrial chemical production.[68,69] In the case of aggregated nanoparticle surfaces, two possible scenarios – interparticle and intraparticle catalytic reactions – exist. Controlled assembly of nanoparticles bearing substrates in the reacting medium can provide a suitable configuration for the molecules to react with each other. Therefore, most of the reported reactions on nanoparticle surfaces are interparticle in nature, which has applications in the formation of assemblies of nanoparticles.[70] The photochemical oxidative dimerization of 4-aminothiophenol (4-ATP) on a nanoparticle surface is a versatile and well-studied reaction that can occur depending on various conditions.[71] The most common dimerization product is 4,4′-dimercaptoazobenzene (DMAB), formed through the coupling of the two aromatic rings *via* an N═N bond.[29] Recently, the interparticle reaction of 4-ATP to DMAB, following organization of an end-to-end assembly of Au nanorods, has been reported.[71] During evaporation of the droplet, nanoparticles bearing shells of water come close to each other at the TPCL. Phase transition also implies the formation of a plasmonic 'hot-spot' at a certain time when molecule-laden nanoparticles come to the closest proximity possible.[40] At this moment, plasmonic photodimerization of 4-ATP through intraparticle mode is possible on the surface of the nanoparticles, and, at the last step of drying, we can monitor the interparticle dimerization after complete loss of the water shell around the 4-ATP between every nanoparticle. In other words, enhanced solvent evaporation at the TPCL drives the loss of solvent molecules from the deposited aggregated nanoparticles. In this regard, the water molecules hydrogen-bonded to the 4-ATP molecules on the same nanoparticle move out first, leading to the intrananoparticle dimerization reaction. This is followed by the loss of water hydrogen-bonded to two or more nanoparticles, leading to an internanoparticle reaction. The above conclusions are substantiated by the experimental evidence presented in the following two sections.

4.1. Isotope effect on the deposition kinetics of nanoparticles functionalized with chemically reacting molecules

In the experimental study, using a setup similar to that in Fig. 2 and a dispersion at pH 7.0, we probed the evaporation of droplets at the TPCL containing 4-ATP-attached spherical silver nanoparticles (ATP@AgNPs) by Raman spectroscopy.[34] The incident laser beam also acted as the photon source to initiate the plasmon-catalyzed photochemical dimerization. The phase transition leading to deposition of AgNPs and the product DMAB formation (or N═N bond formation) were monitored by following the intensity change of the 1078 cm^{-1} (combined C═C and C–S stretching vibration mode) and 1434 cm^{-1} (N═N stretching mode) Raman peaks, respectively, with time.[72] To examine the kinetic isotope effect of the chemical reaction during evaporation, we used H_2O and D_2O solvents. The Raman spectra recorded at different times and the Raman signal intensity change with time for the evaporating droplets of ATP@AgNPs in H_2O and D_2O solvents are shown in Fig. 6.

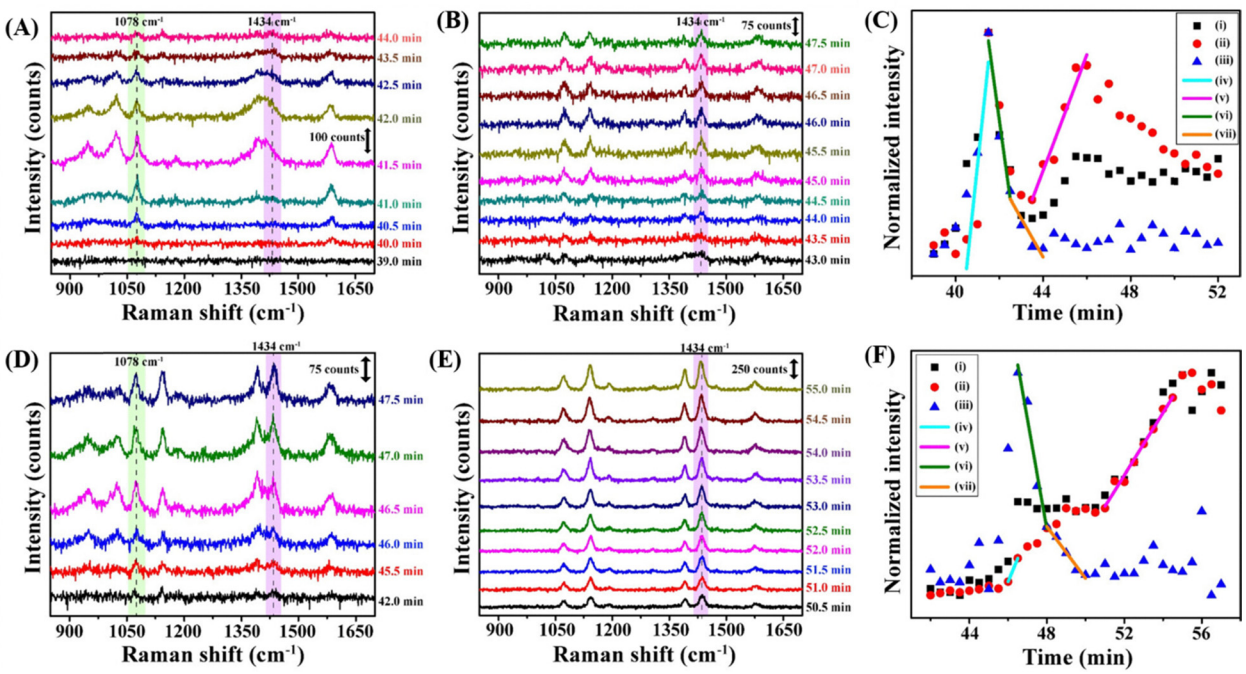

Fig. 6 (A) and (B) Raman spectra at the TPCL of an evaporating droplet at different times for an ATP@AgNP dispersion in H_2O and (C) corresponding variations of (i) 1078, (ii) 1434, and (iii) 946 cm^{-1} Raman peak intensities with time. Linear fittings of the variations of intensities with time for 1434 cm^{-1} (iv) and (v) and 946 cm^{-1} (vi) and (vii) peaks in panel (C). (D) and (E) Raman spectra at the TPCL of an evaporating droplet at different times for an ATP@AgNP dispersion in D_2O and (F) corresponding variations of (i) 1078, (ii) 1434, and (iii) 949 cm^{-1} Raman peak intensities with time. Linear fittings of the variations of intensities with time for the 1434 cm^{-1} (iv) and (v) and 949 cm^{-1} (vi) and (vii) peaks in panel (F). Reproduced with permission from ref. 41; Copyright 2024, the American Chemical Society.

Similar to the previous sections, the 1078 cm^{-1} Raman peak started to appear after 39.0 min (Fig. 6A) and 45 min (Fig. 6D) evaporation time from droplets of H_2O and D_2O, respectively. The intensity of the 1078 cm^{-1} peak increased sharply in both cases, representing the phase transition of ATP@AgNPs from dispersion to deposit at the TPCL (Fig. 6C and F). As shown in Fig. 6C and F, the product formation or the peak at 1434 cm^{-1} started to appear 1.0 min after the start of the phase transition. Then, the intensity of the 1434 cm^{-1} peak jumped in two steps, from 40.0 min to 41.0 min and from 44.0 min to 46.0 min in H_2O (Fig. 6C), and from 46.0 min to 48.5 min and from 51.0 min to 55.0 min in D_2O solvent (Fig. 6F). Therefore, the dimerization product, DMAB, formed in two steps after the phase transition. The rate of DMAB formation in the 1st step was higher than that in the 2nd step in H_2O; however, both rates were comparable in D_2O.

4.2. Two-step release of H-bonded water molecules and subsequent product formation

When the 4-ATP dimerization reaction is carried out in water, water molecules that are H-bonded to the amine group of the 4-ATP molecules that are attached to the nanoparticles should be released prior to the reaction. The thiol group remains bonded to the nanoparticle surface during the process. As the DMAB formation reaction proceeds in two steps, as discussed before, the release of H-bonded water molecules ought to be a two-step process; one prior to intrananoparticle dimerization and the second prior to internanoparticle dimerization of 4-ATP. Thus, while monitoring the progress of 4-ATP dimerization at the TPCL of the evaporating droplet containing ATP@AgNP, detachment kinetics of the H-bonded water molecules from 4-ATP can also be simultaneously distinguished in the two reaction steps.

Interestingly, we also observed the appearance and then disappearance of a peak at 946 cm^{-1} in H_2O and 949 cm^{-1} in D_2O, as shown in Fig. 6C and F, respectively. In both cases, the intensity of these two peaks suddenly increased during the nanoparticle phase transition time window, followed by a two-step decrease in intensity. The initial step of lowering intensity was faster than the 2nd step of lowering intensity. Density functional theory (DFT) calculations revealed that these two Raman signals were due to the collective vibration of 4-ATP and H-bonded solvent molecules.[34] During droplet evaporation, the bulk solvent molecules continuously leave the system; hence, there is an outward pull of the solvent molecules from the surface of the nanoparticles to the bulk. H-bonding energy calculations by the DFT method suggested that the faster step of lowering the peak intensity was because of the cleavage of the H-bonded solvent molecules from the 4-ATP molecules that were attached to the 4-ATP molecules of the same nanoparticle prior to intrananoparticle 4-ATP dimerization.[41] The slower 2nd step decrease of the intensity was due to the loss of internanoparticle solvent molecules that were H-bonded to 4-ATP molecules from two AgNPs, leading to internanoparticle 4-ATP dimerization.[41]

4.3. Mechanisms of intrananoparticle and internanoparticle reactions

The process begins with the ATP@AgNPs undergoing a phase change from a dispersed state to a solid deposit. In the solid, individual AgNPs are close to each other, but still surrounded by a shell of solvent molecules in the milieu of the evaporating droplet (Fig. 7A). As the droplet evaporates, the solvent molecules located between and H-bonded to the intrananoparticle 4-ATP molecules on each AuNP surface move toward the bulk of the droplet (Fig. 7C). This is followed by intrananoparticle DMAB formation (Fig. 7D) in the presence of the probe radiation, while internanoparticle solvent molecules remain within the plasmonic 'hot-spot' regions (Fig. 7E). Next, these remaining internanoparticle solvent molecules move to the bulk (Fig. 7F), allowing for internanoparticle DMAB formation (Fig. 7G). The final steps involve the evaporation of the remaining bulk solvent molecules (Fig. 7H), leaving behind a completely dry deposit of DMAB-attached AgNPs (DMAB@AgNPs) (Fig. 7I). The droplet evaporation-induced particle deposition technique is the only possible way reported so far for the distinction of intrananoparticle and internanoparticle plasmon-catalyzed reactions. The ratio of the intrananoparticle and internanoparticle 4-ATP dimerization was 3.0 and 1.8 in H_2O and D_2O medium, respectively.

5. Three distinct pH-controlled stepwise depositions across the annulus of the ring

Surface chemical functionalization is important in tailoring nanoparticles for a wide range of applications that require enhanced stability, emergent physical and chemical properties, improved biocompatibility and environmental friendliness.[32,33] The precision in the arrangements of functionalized nanoparticles into well-defined arrays is important in the field of droplet-based printing technology for device fabrication.[73] The applications of those functionalized nanoparticles are remarkably influenced by the properties of the chemical environment in which they are present. In aqueous dispersions, the pH of the medium is a major factor controlling the stability and reactivity of the nanoparticles.[74–76] Moreover, the kinetics of the evaporation-induced particle deposition and subsequent chemical reaction may also be influenced at the three distinct boundary regions of the TPCL, namely, the outer, middle and inner boundaries. The capillary forces, interfacial tension and viscous forces dictate how microparticles are transported to and deposited at the TPCL.[77] However, for functionalized nanoparticles in a chemically reacting medium with hydrogen bonds between the solvent and the surface-attached molecules, the deposition process is more complex, and conventional techniques cannot follow the deposition as well as the chemical reactions simultaneously. By utilizing SERS, the effects of pH on the dimerization of 4-ATP on the AgNP surfaces (interfaces) and the different depositions across the annulus of the ring have been monitored simultaneously.[42]

5.1. Effect of pH on deposition mechanism

At pH 7.0, the ATP@AgNPs were deposited through a single phase transition and, following this, the DMAB formation was

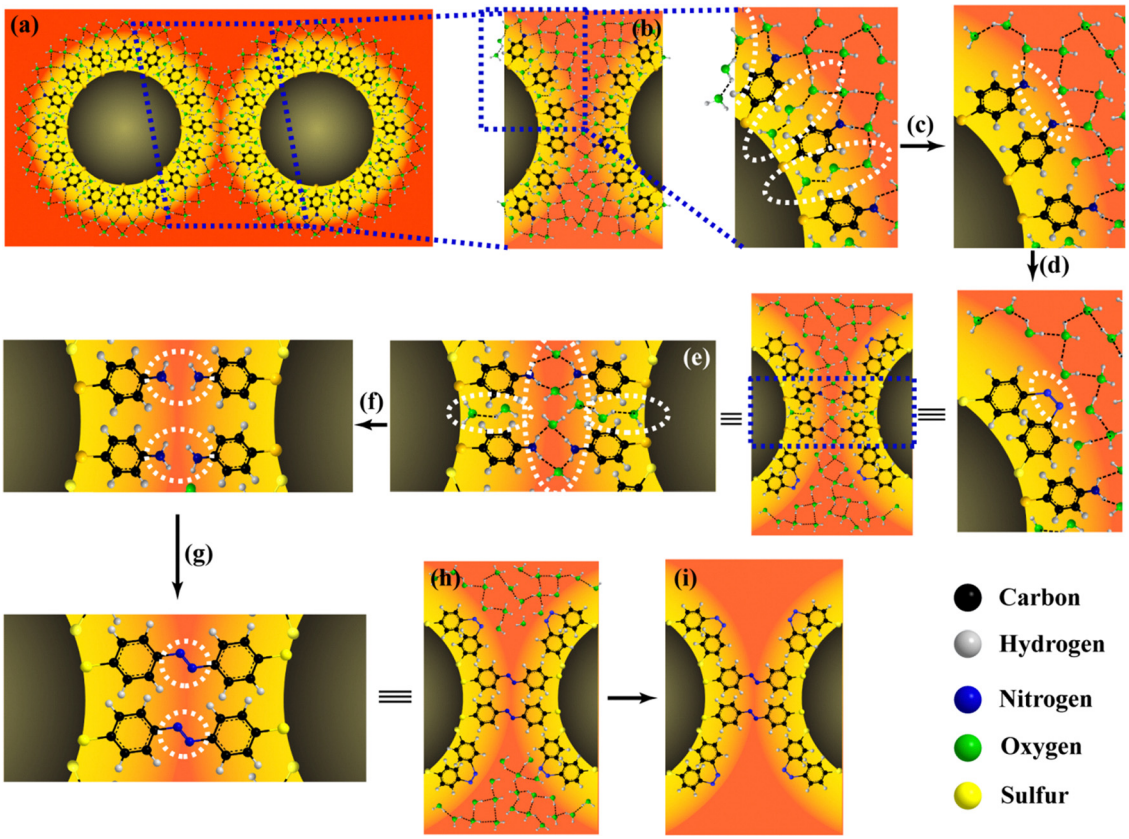

Fig. 7 (A) Two-dimensional schematic of two ATP@AgNPs with solvent shells connected through H-bonds, with (B) the cross-sectional area indicated in panel (A), showing the solvent network attached to 4-ATP between the two AgNPs. (C) Loss of intrananoparticle solvent molecules (marked) between 4-ATP molecules closest to the NP surface. (D) Intrananoparticle DMAB formation. (E) Cross-section area showing internanoparticle solvent molecules attached to 4-ATP through H-bonds. (F) Loss of internanoparticle solvent molecules (marked). (G) Internanoparticle DMAB formation. (H) Representation of DMAB@AgNP with bulk solvent molecules in the surroundings. (I) Fully dried DMAB@AgNP. Reproduced with permission from ref. 41; Copyright 2024, the American Chemical Society.

completed in two steps (Fig. 8A and B). As discussed earlier, the initial faster product formation was intrananoparticle DMAB formation and the slower 2nd step corresponded to internanoparticle DMAB formation.[42] Interestingly, different results were obtained at pH 8.4 and 9.4. At pH 8.4, Raman signal intensity increased in six steps during the time intervals 32.0 min to 32.75 min, 33.75 min to 34.25 min, 35.75 min to 36.75 min, 37.0 min to 38.25 min, 39.0 min to 39.75 min, and 40.25 min to 41.0 min (Fig. 8C and D). These stepwise jumps in signal intensity indicated a multistep deposition process, where the nanoparticles were deposited from the dispersed phase to the solid at the TPCL. As the 4-ATP dimerization reaction rate is higher at pH 8.4 compared to that at pH 7.0, DMAB formation at the TPCL of the droplet of ATP@AgNPs at pH 8.4 also simultaneously occurred in six steps, accompanying the phase transitions. At pH 9.4, a single phase transition was noticed from 30.5 min to 33.5 min, indicated by a sudden jump in intensities of the 1078 cm^{-1} and 1434 cm^{-1} Raman peaks (Fig. 8E and F). Unlike at lower pH values, the DMAB product (indicated by the 1434 cm^{-1} peak) formed earlier, from 25.0 min to 29.0 minutes, in the dispersion itself before deposition had occurred (Fig. 8F(iii)). This early DMAB formation is attributed to the high pH, which accelerates the dimerization of 4-ATP. Consequently, the phase transition involved the deposition of DMAB-coated AgNPs (DMAB@AgNPs) at the TPCL from the dispersion phase.

5.2. Dependence of the nanoparticle deposition kinetics on the location of the probe area

In order to understand the kinetics as well as the deposition of the nanoparticles across the locations corresponding to the annulus of the ring, Raman measurements were carried out at three distinct probe areas, namely, the outer, middle, and inner boundaries.[42] At pH 7.0, in all three spots, the nanoparticles were deposited in a single phase transition from dispersion to deposit, followed by intrananoparticle and internanoparticle dimerization of 4-ATP.[42] At pH 9.4, all the 4-ATP molecules on the surface of the AgNPs were dimerized in the dispersion medium long before the phase transition.[42] At this pH, a single phase transition of DMAB@AgNPs was also observed at the three probe areas. However, at pH 8.4, the number of phase transitions and depositions at three probe areas differed. SERS measurements revealed that, at the outer and inner boundaries of the TPCL, three phase transition steps were observed, which

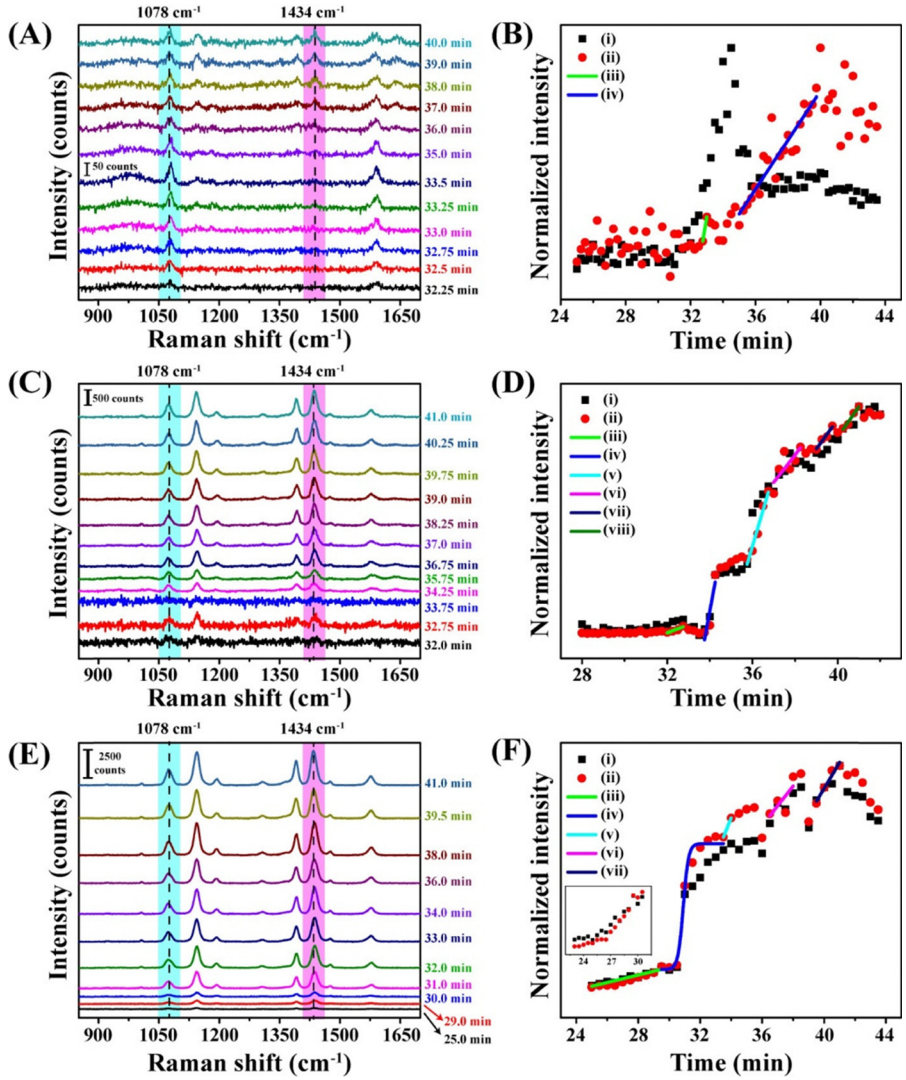

Fig. 8 Raman spectra at different times recorded at the TPCL of evaporating droplets containing ATP@AgNP dispersions at (A) pH 7.0, (C) pH 8.4, and (E) pH 9.4. Variation of (i) 1078 cm^{-1} and (ii) 1434 cm^{-1} Raman peak intensities with time for evaporating droplets containing ATP@AgNPs at (B) pH 7.0, (D) pH 8.4 and (F) pH 9.4. The graphs (iii) and (iv) in (B), (iii) to (viii) in (D), and (iii), (v) to (vii) in (F) are linear fittings of the variations of 1434 cm^{-1} Raman peak intensities with time. The graph (iv) in (F) is a Boltzmann fitting of the variations of the 1434 cm^{-1} Raman peak intensity with time. The inset in (F) is an expanded view of the range from 23 to 30 min. Reproduced with permission from ref. 42; Copyright 2025, the American Chemical Society.

is lower than the six phase transitions or deposition steps at the middle of the TPCL.[42] In order to further confirm the different number of phase transitions and the step-by-step deposition at the three probe areas, AFM measurements were also pursued on the deposit after each phase transition step. The results supported the measurement outcome of SERS on the same spots.

Analysis of the solid deposit at pH 8.4 revealed that its height and width both increased with each phase transition. The deposit height profile plots after each phase transition (Fig. 9A) show a step-by-step increase in deposit height, which was particularly monotonous for the first four steps (Fig. 9B). After the fourth step, the increase in height became less significant. In contrast, the width of the deposit increased linearly with each of the six phase transitions (Fig. 9C). When probed at the outer edge of the deposit, the height was observed to have increased only until the third deposition step, as marked in Fig. 9A. At the inner boundary, the last three phase transitions caused the deposit to grow in width (Fig. 9A). At the middle of the deposit, however, all six phase transitions were clearly identified through SERS measurements, as both height and width changes were measurable. The significant increases in both height and width during the 2nd and 3rd steps indicated that a larger number of nanoparticles were deposited during these two steps.

5.3. Mechanism of reacting nanoparticles deposition at the three pH values

Our experiments suggested that the deposition kinetics of ATP@AgNPs at the TPCL are highly dependent on the pH of the dispersion. The deposition process, shown schematically in Fig. 10, is influenced by three key factors: (i) the rates of advective flow of ATP@AgNPs, which were nearly the same at

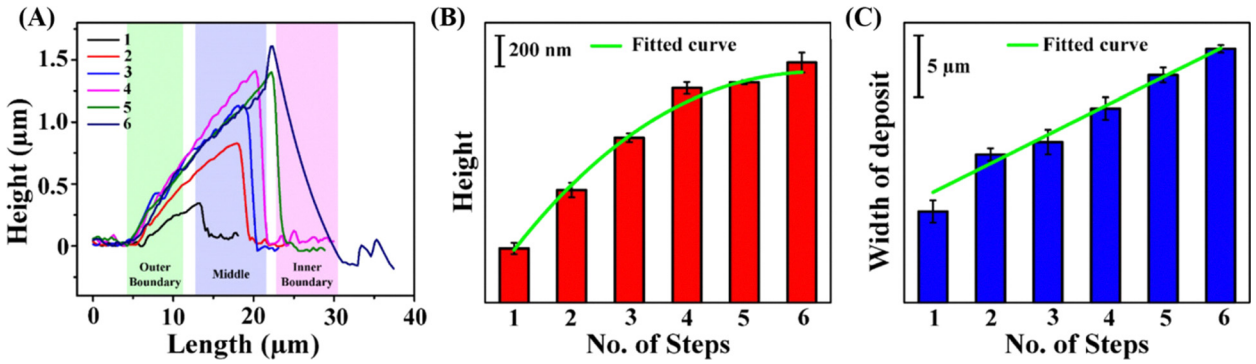

Fig. 9 (A) Height profile diagrams of the dried deposits for the number of phase transitions mentioned in the legends. Raman probe areas are highlighted. Bar diagrams with fitted curves of the (B) height of the deposit and (C) width of the deposit plotted against the phase transition step number. Reproduced with permission from ref. 42; Copyright 2025, the American Chemical Society.

pH 7.0, 8.4 and 9.4, as evidenced by the starting of phase transition at nearly same time of evaporation,[42] (ii) pH-dependent photochemical dimerization of 4-ATP, and (iii) pH dependent kinetic stability of ATP@AgNPs in the dispersions, which we confirmed from zeta potential measurements.[42] With increasing pH values, the ATP@AgNP dispersion became kinetically more stable.[42] The deposition kinetics of ATP@AgNPs at pH 7.0 were straightforward and are discussed in the previous section. ATP@AgNPs are initially deposited as a solid due to their lower kinetic stability (Fig. 10) and DMAB formation starts in two steps (Fig. 10) after the formation of plasmonic 'hot-spots' in the solid deposit due to the otherwise lower rate of chemical reaction. At pH 8.4, due to the moderately higher reaction rate of 4-ATP and the dispersibility of ATP@AgNPs,

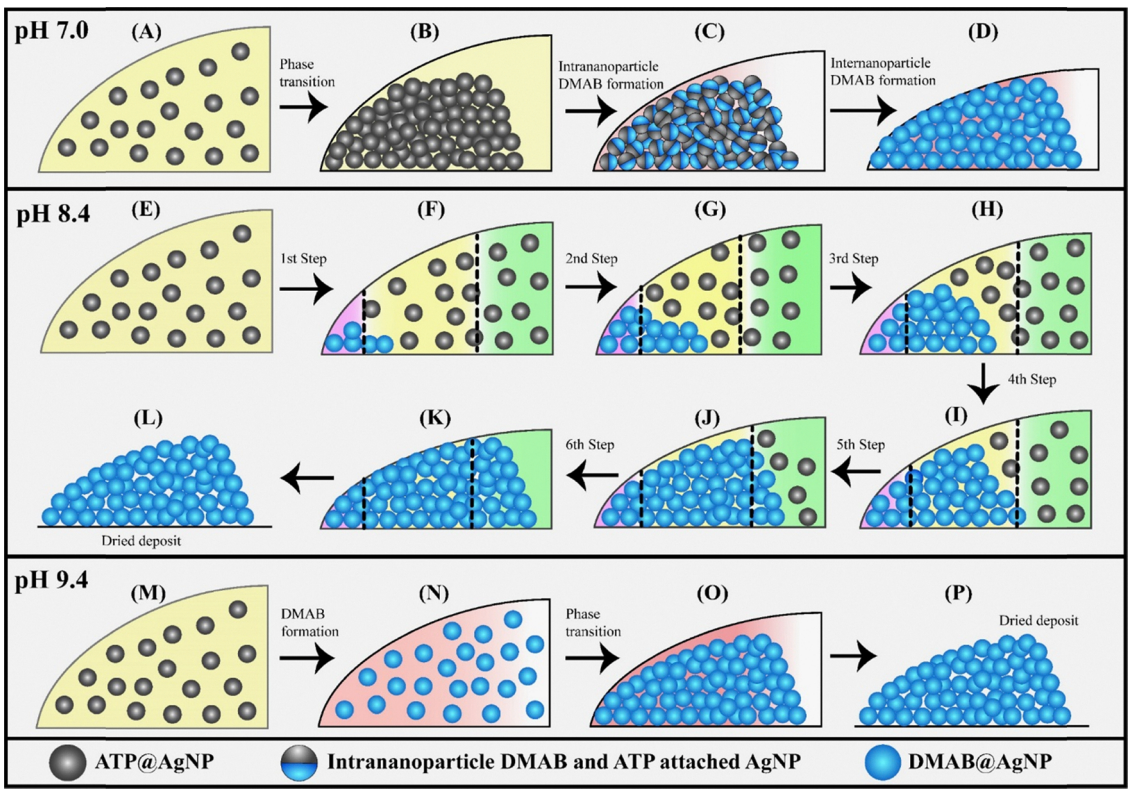

Fig. 10 Two-dimensional schematics of the (A) dispersion of ATP@AgNPs at the TPCL at pH 7.0, (B) deposited ATP@AgNPs after phase transition at pH 7.0, (C) AgNP deposits after the intrananoparticle DMAB formation at pH 7.0, (D) AgNP deposits after the internanoparticle DMAB formation at pH 7.0, and (E) dispersed ATP@AgNPs at the TPCL at pH 8.4. The AgNP deposits after the (F) 1st, (G) 2nd, (H) 3rd, (I) 4th, (J) 5th, and (K) 6th phase-transition steps and simultaneous DMAB formation around AgNPs. Schematic of the (L) dried DMAB@AgNP deposit at pH 8.4. Two-dimensional schematics of the (M) dispersed ATP@AgNP at the TPCL at pH 9.4, (N) dispersed DMAB@AgNPs after photochemical reactions of ATP@AgNPs at the TPCL at pH 9.4, (O) deposited DMAB@AgNPs at the TPCL after single-phase transition at pH 9.4, and (P) dried DMAB@AgNPs deposited at pH 9.4. Reproduced with permission from ref. 42; Copyright 2025, the American Chemical Society.

they remain in the dispersed phase for a sufficiently long time for photochemical dimerization immediately after they reach the TPCL (Fig. 10E). After that, these newly formed product assemblies were deposited at the TPCL, resulting in a sudden jump in Raman signal intensities at both 1078 cm^{-1} and 1434 cm^{-1}. The deposition process at pH 8.4 was observed in multiple steps. Subsequent steps (steps 2–6) demonstrated a sharp rise in the Raman peak intensity (Fig. 8D), particularly in steps 2 and 3, indicating a greater number of particles arriving and reacting faster at the TPCL. This multistep deposition process, as shown in Fig. 10F–K, is driven by photochemical reactions at the TPCL, leading to the agglomeration and sequential deposition of the nanoparticles. As evidenced from the AFM measurements, during the first three steps shown in Fig. 10F–H, both the height and width of the deposit grew significantly as large numbers of nanoparticles were deposited at the outer and middle boundaries. After the 4th step, the deposition of nanoparticles was shifted to the middle and inner boundaries (Fig. 10I). During the step-by-step deposition, the droplet height also decreased due to evaporation of solvent, and, after the 4th step, the solid deposit height reached its maximum value and the movement of more nanoparticles on top of the already deposited solid was not possible. Therefore, during the 5th and 6th steps, the width of the deposit increased significantly. At pH 9.4, as is obvious from Fig. 8F(iii), the rate of DMAB formation was fast, and the dispersion was kinetically stable, so that nearly all the 4-ATP molecules on the ATP@AgNP surface dimerized into DMAB, forming DMAB@AgNPs in the dispersion medium at or near the TPCL, as shown in Fig. 10N. Here, intrananoparticle and internanoparticle reactions could not be distinguished. Because of high dispersibility at pH 9.4, most of the particles deposited in one major phase transition after reaching a certain particle concentration. Hence, we observed one such major phase transition step in Fig. 8F(iv), which is represented schematically in Fig. 10O.

6. Droplet evaporation-induced anomalous two-dimensional molecular crystallization

The development of low-dimensional materials is important for next-generation technological applications, such as flexible electronics, quantum materials, advanced sensors, chemical catalysis and theranostics.[78–83] Molecular crystals have shown potential applications in the formation of SERS substrates with selectivity and specificity, and in the fabrication of two-dimensional (2D) moiré superlattices for sensing, catalysis, and quantum materials.[38,39,84–86] Despite the numerous methodologies that are known for three-dimensional (3D) crystal growth, techniques for systematically growing one-dimensional or 2D molecular crystals from solution remain a challenge and are not yet fully developed. Recently, we developed a method for achieving 2D molecular crystal growth by using evaporation-induced deposition at the TPCL of a droplet starting from a solution of the molecule.[43] Crystallization of the organic molecules methyl orange (MO) and methylene blue (MB) was pursued by evaporating sessile droplets of solutions of each molecule on a glass slide. The crystallization process was monitored at the TPCL by following a jump in the Raman signal intensity of the analyte molecule due to solidification from the solution phase and deposition of microcrystals, as shown in Fig. 11.[43]

For further analysis of the nature of the solid deposit and to determine the molecular arrangements, powder X-ray diffraction measurements on the thin film after complete evaporation

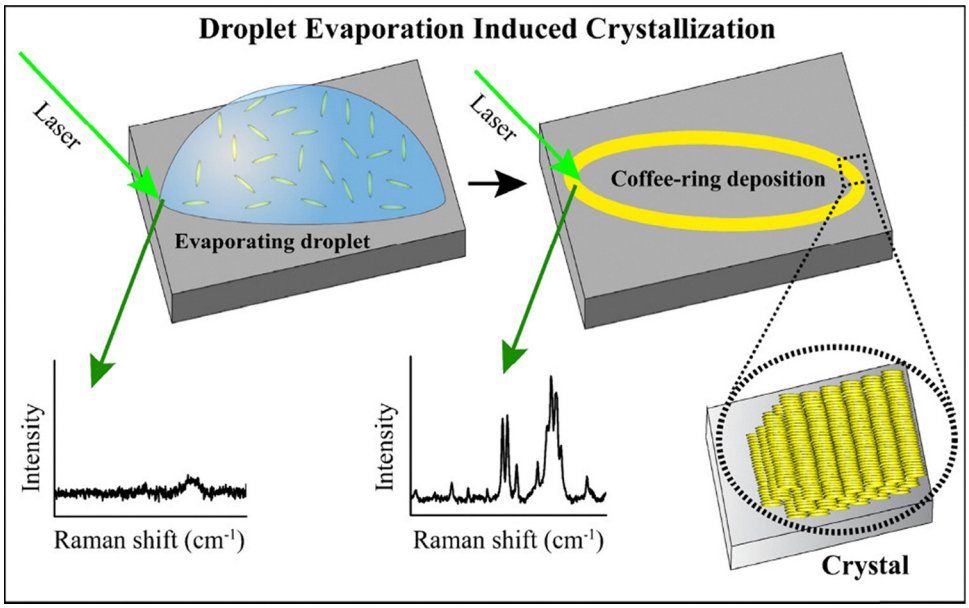

Fig. 11 Schematic of the Raman spectroscopic measurements at the TPCL of the evaporating droplet, leading to evaporation-induced crystallization of the dissolved molecules. Reproduced with permission from ref. 40; Copyright 2025, the American Chemical Society.

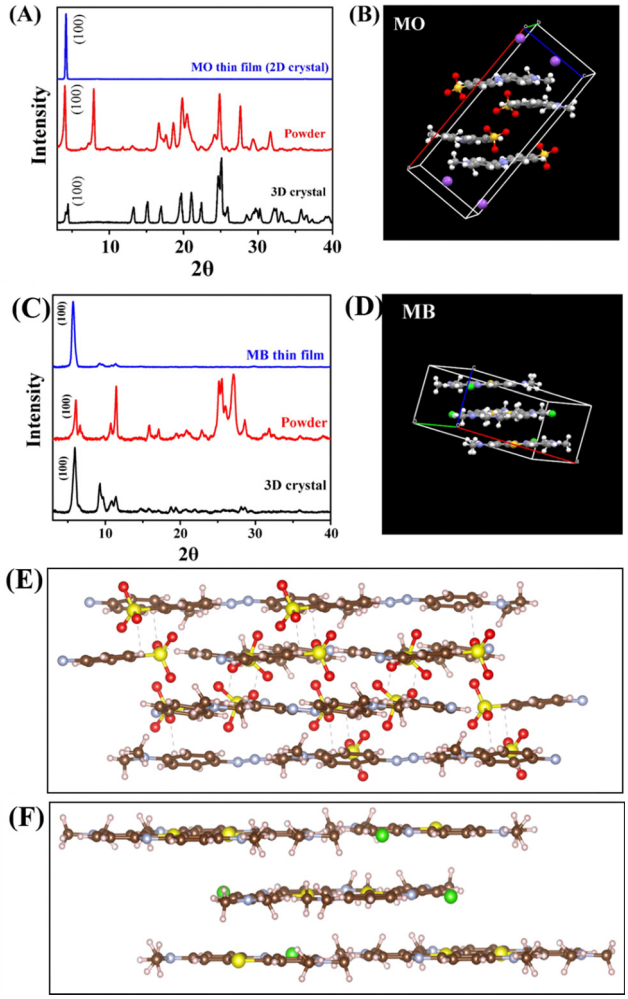

Fig. 12 (A) Powder XRD pattern of the bulk MO crystal (black), the MO powder (red), and the MO thin film (blue) obtained after evaporation of a droplet of MO solution. (B) Crystal structure of MO after refinement of the powder XRD pattern of the thin film. Gray, white, light blue, red, yellow, and violet atoms represent C, H, N, O, S, and Na atoms, respectively. (C) Powder XRD patterns of the bulk MB crystal (black), MB powder (red) and the MB thin film (blue) obtained after evaporation of droplets of MB solution. (D) Crystal structure of MB after refinement of the powder XRD pattern of the thin film. 2D layer-by-layer arrangement of (E) MO and (F) MB molecules in the crystal. Brown, white, pale blue, red, light yellow and green atoms are C, H, N, O, S and Cl atoms, respectively. Reproduced with permission from ref. 43; Copyright 2025, the American Chemical Society.

were carried out. As shown in Fig. 12A, it is clear that the XRD pattern of the MO thin film consisted of only one major diffraction peak at 4.2° (2θ). Powder XRD measurement of the MB thin film revealed only one major diffraction peak at 5.7° (2θ) and two minor reflections at 9.3° and 11.3° (Fig. 12C). The existence of only one major peak implied the selective growth of only one crystalline plane. After comparing the powder XRD data of the thin films with the bulk 3D crystals, it was found that only the (100) plane grew for both the MO and MB thin films. Theoretical refinement using the experimentally obtained XRD data confirmed the layer-by-layer arrangements of both MO and MB molecules in the thin film (Fig. 12B and D). Furthermore, the layer-by-layer structures of both MO and MB were seen in their respective crystals, as shown in Fig. 12E and F. The layers are stacked in a 2D fashion. Importantly, the 2D crystal structures differed from their 3D counterparts. For example, the MO 2D crystal belongs to the $P2_1/c$ space group, with lattice parameters 20.0 Å (a), 9.3 Å (b) and 8.3 Å (c), but the cell parameters of the 3D MO crystals are 22.11 Å (a), 10.34 Å (b) and 8.3 Å (c). Moreover, the diffraction at 4.2° (2θ) for the (100) plane is shifted to 4.46° for the 3D crystal and the MO molecules in the adjacent layers are perpendicular to each other. For MB, the 2D crystal is composed of parallel layers of MB molecules.

7. Different vibrational signatures of molecules at the surface and interior of the crystals

Raman measurements on the surface and interior of the 2D crystals revealed that the vibrational characteristics of molecules at the surface and interior were different.[43] When the evaporation-generated crystals were etched either by laser light or mechanically, the Raman signal intensities increased for both MO and MB. In other words, the signal intensities for the interior vibrations were higher than those on the surfaces. In addition to the intensity enhancement, peak position shifts of several vibrational modes were observed. This phenomenon was also confirmed from DFT calculations of the Raman spectra using the optimized structures of the molecule at the surface and interior of each crystal. In case of MO 2D crystal, in the experimental spectra as shown in Fig. 13A, the Raman peaks at 932, 1120, 1152, 1202, 1317 and 1394 cm^{-1} were redshifted to 923, 1117, 1143, 1195, 1313 and 1389 cm^{-1}, respectively. All these Raman peaks have a common δ(C–H) vibrational mode.[36] The DFT-optimized structure suggested that the extent of the C–H$\cdots$O interaction is higher for molecules in the interior of the 2D crystal compared to those at the surface. The greater extent of the C–H$\cdots$O interactions is the main reason for the redshift of the Raman signal on moving from the surface to the interior, which was also confirmed by the calculated Raman spectra shown in Fig. 13B.[87] Our further studies of the MB 2D crystal revealed that the Raman signal corresponding to ν(C–N) at 1398 cm^{-1} was red shifted to 1393 cm^{-1} on moving from the surface to the interior. The C–N bond length (1.41 Å) on the inside of the MB 2D crystal was higher than the C–N bond length of 1.35 Å at the surface of the crystal. This increased bond length resulted in the redshift of the vibrational Raman mode.[88] However, in the case of the 3D crystal of MO, the Raman peak at 1116 cm^{-1}, corresponding to the ν(Ph–N) + δ(C–H) vibration at the surface, was blueshifted to 1119 cm^{-1} in the interior, due to the shortening of the Ph–N bond length in the interior (1.397 Å) relative to the 1.407 Å bond length at the surface.[43,88] Similar to the MB 2D crystal, in the case of the MB 3D crystal, due to the increase in the C–N bond length on going from the surface to the interior, the Raman peak at 1397 cm^{-1}, corresponding to the ν(C–N) vibration, was

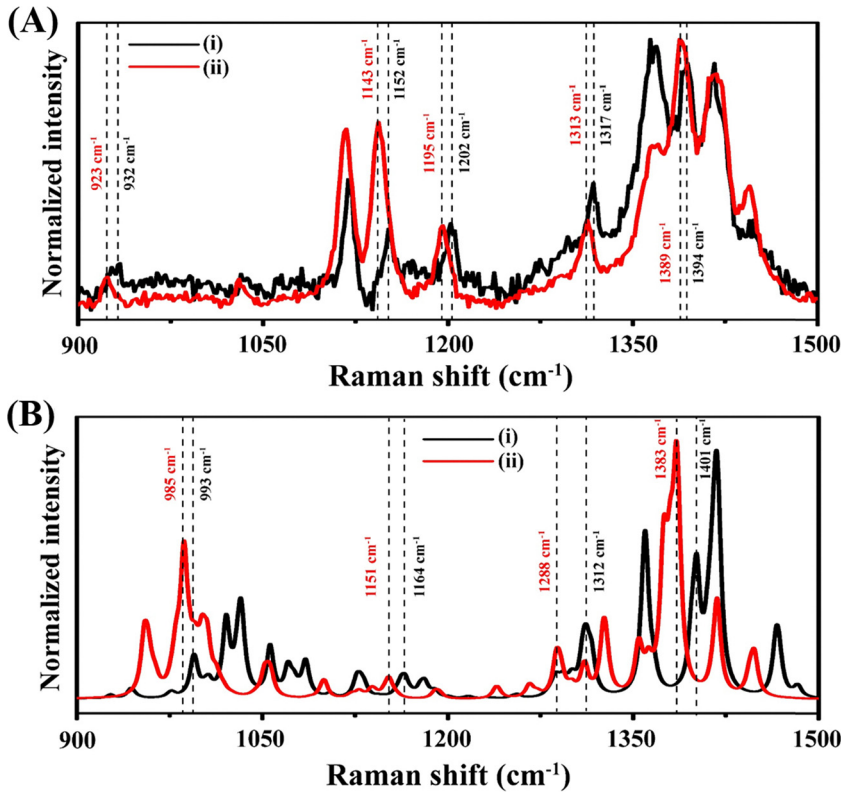

Fig. 13 (A) Experimental Raman spectra and (B) calculated Raman spectra, showing different peak positions of MO on the (i) smooth surface of the crystal and (ii) etched surface or inside the crystal. Reproduced with permission from ref. 43; Copyright 2025, the American Chemical Society.

redshifted to 1390 cm^{-1} on moving from the surface to the interior.[43,88] The results indicated that the surface vibrations of a molecular crystal (either 2D or 3D) are fundamentally different from those in the interior of the crystal.

8. Conclusions

Our laboratory's exploration of the chemistry of evaporation-induced particle deposition, as reported herein, has greatly improved our understanding of the deposition kinetics of nanoparticle systems. The deposition characteristics of nanoparticles at the TPCL of evaporating droplets were monitored using the vibrational characteristics of molecules used for the chemical stabilization of the surface of nanoparticles. For the first time, utilizing SERS as a spectroscopic probe for the functionalized molecules, we discovered that the nanoparticles in a non-reacting environment follow a single phase transition from dispersion to deposition during the evaporation of nanoparticle-laden sessile droplets. The generation of plasmonic 'hot-spots', which is reflected in the sudden rise in SERS intensity for the solid deposit, played a crucial role in distinguishing the two separate phases. However, there was a pH-dependent behavior that revealed the possibility of multiple phase transitions in the deposition steps. The deposition kinetics of plasmonic nanoparticles also helped in understanding novel chemical phenomena around the nanoparticles. For example, the distinction between intrananoparticle and internanoparticle photochemical reactions was discovered by following the phase transition behavior. Additionally, 2D crystals of MO and MB molecules could be made by the droplet evaporation-induced deposition technique. Further analysis by Raman spectroscopy also suggested that the surface of the crystals is different from the interior at the molecular vibrational level.

The discovery of novel phase-transition behavior of nanoparticles at the TPCL during 'coffee-ring' pattern formation significantly broadens our chemical understanding of natural fundamental processes. This remarkable progress can be used to obtain new information about other heterogeneous chemical reactions around the surface of nanoparticles. The ability to separate intra- and internanoparticle plasmonic reactions provides a blueprint for adaptive manufacturing. Future visions involve the use of evaporation-driven mechanisms for creating self-repairing surfaces and inkjet-printed SERS substrates with optimized 'hot-spots'. Our research on the effect of pH and surface functionalization will provide chemical clues to reproducible printing of particles through the evaporation of droplets. The transition of the molecular solution inside droplets into highly ordered 2D crystals is expected to be useful for the production of organic flexible displays and wearable biosensors. These studies of nanoparticle deposition leading to 'coffee-ring' formation could spur new discoveries in liquid-based printing, forensics, and agriculture. The droplet evaporation-induced 2D crystallization may be an important technique for the facile

preparation of molecular moiré superlattices that are turning out to be as important as quantum matter. Thus, the potential of the field is open to exploration.

Conflicts of interest

The authors declare no competing financial interest.

Data availability

No primary research results, software or code have been included and no new data were generated or analyzed in the feature article. The content in Fig. 1 is a scheme with no primary data.

Acknowledgements

We thank the Ministry of Electronics and Information Technology, Government of India (MEITY grant no. 5(1)/2022- NANO), for financial support. AC thanks the Anusandhan National Research Foundation (ANRF), Government of India, for a J. C. Bose Fellowship (ANRF/JBG/2025/000034/CS).

References

1 X. Kong, Y. Xi, P. LeDuff, E. Li, Y. Liu, L. Cheng, G. Rorrer, H. Tan and A. X. Wang, *Nanoscale*, 2016, **8**, 17285–17294, DOI: 10.1039/C6NR05809D.
2 J. Schneider, P. Rohner and P. Galliker, *et al.*, *Nanoscale*, 2015, **7**, 9510–9519, DOI: 10.1039/C5NR01314K.
3 X. Du, S. P. Wankhede and S. Prasad, *et al.*, *J. Mater. Chem. C*, 2022, **10**, 14091–14115, DOI: 10.1039/D2TC02511F.
4 S. Bhattacharjee, N. P. Vaisakh, S. Khawas, U. Afnan and S. Srivastava, *J. Phys.: Condens. Matter*, 2026, **38**, 063001, DOI: 10.1088/1361-648X/ae2c31.
5 N. Bridonneau, M. Zhao, N. Battaglini, G. Mattana, V. Thévenet, V. Noël, M. Roché, S. Zrig and F. Carn, *Langmuir*, 2020, **36**(39), 11411–11421, DOI: 10.1021/acs.langmuir.0c01546.
6 J. Ren, A. Crivoi and F. Duan, *Phys. Chem. Chem. Phys.*, 2021, **23**, 15774–15783, DOI: 10.1039/D1CP01181B.
7 R. Malinowski, G. Volpe, I. P. Parkin and G. Volpe, *J. Phys. Chem. Lett.*, 2018, **9**(3), 659–664, DOI: 10.1021/acs.jpclett.7b02831.
8 R. A. O'Connell, W. N. Sharratt and J. T. Cabral, *Phys. Rev. Lett.*, 2023, **131**, 218101, DOI: 10.1103/PhysRevLett.131.218101.
9 S.-H. Hung, Y.-H. Lin and G.-B. Lee, *J. Micromech. Microeng.*, 2010, **20**, 045026, DOI: 10.1088/0960-1317/20/4/045026.
10 A. Yousfan, N. Moursel and A. Hanano, *Sci. Rep.*, 2024, **14**, 32057, DOI: 10.1038/s41598-024-83715-7.
11 N. Shahidzadeh, M. F. L. Schut and J. Desarnaud, *et al.*, *Sci. Rep.*, 2015, **5**, 10335, DOI: 10.1038/srep10335.
12 A. Susarrey-Arce, A. Marin and A. Massey, *et al.*, *Langmuir*, 2016, **32**, 7159–7169, DOI: 10.1021/acs.langmuir.6b01658.
13 L. Nayak, S. Mohanty and S. K. Nayak, *et al.*, *J. Mater. Chem. C*, 2019, **7**, 8771–8795, DOI: 10.1039/C9TC01630A.
14 Y. Liu, H. Zhu and L. Xing, *et al.*, *Nanoscale*, 2023, **15**, 6025–6051, DOI: 10.1039/D2NR05649F.
15 T.-T. Huang and W. Wu, *J. Mater. Chem. A*, 2019, **7**, 23280–23300, DOI: 10.1039/C9TA05239A.
16 Z. Bashiri, I. Amiri and M. Gholipourmalekabadi, *et al.*, *Biomater. Sci.*, 2021, **9**, 3465–3484, DOI: 10.1039/D0BM02209H.
17 A. Olejnik, J. A. Semba and A. Kulpa, *et al.*, *ACS Synth. Biol.*, 2022, **11**, 26–38, DOI: 10.1021/acssynbio.1c00547.
18 S. Kim, J. J. Handler and Y. T. Cho, *et al.*, *Sci. Adv.*, 2021, **7**, eabh1200, DOI: 10.1126/sciadv.abh1200.
19 D. Lohani, M. G. Basavaraj, D. K. Satapathy and S. Sarkar, *Colloids Surf., A*, 2020, **589**, 124387, DOI: 10.1016/j.colsurfa.2019.124387.
20 P. J. Yunker, T. Still, M. A. Lohr and A. G. Yodh, *Nature*, 2011, **476**, 308–311, DOI: 10.1038/nature10344.
21 R. Tao, Z. Fang and J. Zhang, *et al.*, *ACS Appl. Mater. Interfaces*, 2018, **10**, 22883–22888, DOI: 10.1021/acsami.8b06519.
22 W. Zhang, T. Yu, L. Liao and Z. Cao, *AIP Adv.*, 2013, **3**, 102109, DOI: 10.1063/1.4824741.
23 D. Brutin, *Colloids Surf., A*, 2013, **429**, 112–120, DOI: 10.1016/j.colsurfa.2013.03.012.
24 R. D. Deegan, O. Bakajin, T. F. Dupont, G. Huber, S. R. Nagel and T. A. Witten, *Nature*, 1997, **389**, 827–829, DOI: 10.1038/39827.
25 R. D. Deegan, O. Bakajin, T. F. Dupont, G. Huber, S. R. Nagel and T. A. Witten, *Phys. Rev. E:Stat. Phys., Plasmas, Fluids, Relat. Interdiscip. Top.*, 2000, **62**, 756–765, DOI: 10.1103/PhysRevE.62.756.
26 F. Boulogne, F. Ingremeau and H. A. Stone, *J. Phys.: Condens. Matter*, 2017, **29**, 074001, DOI: 10.1088/1361-648X/aa5160.
27 C. de Blois, M. Engel and C. N. Jones, *Lab Chip*, 2020, **20**, 3687–3697, DOI: 10.1039/D0LC00506A.
28 L. Xu, W. Ma, L. Wang, C. Xu, H. Kuang and N. A. Kotov, *Chem. Soc. Rev.*, 2013, **42**, 3114–3126, DOI: 10.1039/c3cs35460a.
29 S. Pal, S. Paul and A. Chattopadhyay, *Phys. Chem. Chem. Phys.*, 2021, **23**, 21808–21816, DOI: 10.1039/D1CP02931B.
30 K. Bhattacharjee and B. L. V. Prasad, *Chem. Soc. Rev.*, 2023, **52**, 2573–2595, DOI: 10.1039/D1CS00876E.
31 T. Bian, A. Gardin, J. Gemen, L. Houben, C. Perego, B. Lee, N. Elad, Z. Chu, G. M. Pavan and R. Klajn, *Nat. Chem.*, 2021, **13**, 940–949, DOI: 10.1038/s41557-021-00752-9.
32 L. Xu, H.-W. Liang, Y. Yang and S.-H. Yu, *Chem. Rev.*, 2018, **118**, 3209–3250, DOI: 10.1021/acs.chemrev.7b00208.
33 F. Mazzotta, S. Pottanam Chali, I. Lieberwirth, C. T. J. Ferguson and K. Landfester, *Polym. Chem.*, 2025, **16**, 433–440, DOI: 10.1039/D4PY01119H.
34 V. Amendola, R. Pilot, M. Frasconi, O. M. Maragò and M. A. Iatì, *J. Phys.: Condens. Matter*, 2017, **29**, 203002, DOI: 10.1088/1361-648X/aa60f3.
35 A. Dutta and A. Chattopadhyay, *J. Phys. Chem. C*, 2017, **121**, 18854–18861, DOI: 10.1021/acs.jpcc.7b06889.
36 J. Yi, E.-M. You and R. Hu, *et al.*, *Chem. Soc. Rev.*, 2025, **54**, 1453–1551, DOI: 10.1039/D4CS00883A.
37 C. Deriu and L. Fabris, *Chem. Soc. Rev.*, 2025, **54**, 5224–5247, DOI: 10.1039/D4CS01242A.
38 A. Bhakat, S. Paul and A. Chattopadhyay, *J. Phys. Chem. C*, 2023, **127**, 5169–5177, DOI: 10.1021/acs.jpcc.2c07663.
39 A. Bhakat and A. Chattopadhyay, *Adv. Opt. Mater.*, 2024, **12**, 2301776, DOI: 10.1002/adom.202301776.
40 S. Paul and A. Chattopadhyay, *J. Phys. Chem. C*, 2023, **127**, 22401–22411, DOI: 10.1021/acs.jpcc.3c06159.
41 S. Paul and A. Chattopadhyay, *J. Phys. Chem. Lett.*, 2024, **15**, 6812–6817, DOI: 10.1021/acs.jpclett.4c01741.
42 S. Paul and A. Chattopadhyay, *J. Phys. Chem. C*, 2025, **129**, 4250–4260, DOI: 10.1021/acs.jpcc.4c09068.
43 S. Paul and A. Chattopadhyay, *J. Phys. Chem. Lett.*, 2025, **16**, 7428–7435, DOI: 10.1021/acs.jpclett.5c01625.
44 H. Y. Erbil, G. McHale and M. I. Newton, *Langmuir*, 2002, **18**(7), 2636–2641, DOI: 10.1021/la011470p.
45 A. H. Govindha, S. Banerjee, S. Balusamy and K. C. Sahu, *Langmuir*, 2025, **41**(45), 30562–30572, DOI: 10.1021/acs.langmuir.5c04303.
46 H.-J. Butt, D. S. Golovko and E. Bonaccurso, *J. Phys. Chem. B*, 2007, **111**, 5277–5283, DOI: 10.1021/jp065348g.
47 S. M. Rowan, M. I. Newton and G. McHale, *J. Phys. Chem.*, 1995, **99**(35), 13268–13271, DOI: 10.1021/j100035a034.
48 C. Bourges-Monnier and M. E. R. Shanahan, *Langmuir*, 1995, **11**(7), 2820–2829, DOI: 10.1021/la00007a076.
49 H. Hu and R. G. Larson, *J. Phys. Chem. B*, 2002, **106**, 1334–1344, DOI: 10.1021/jp0118322.
50 R. G. Picknett and R. Bexon, *J. Colloid Interface Sci.*, 1977, **61**(2), 336–350, DOI: 10.1016/0021-9797(77)90396-4.
51 D. M. Soolaman and H.-Z. Yu, *J. Phys. Chem. B*, 2005, **109**(38), 17967–17973, DOI: 10.1021/jp051182s.
52 Y. Zhang, X. Chen, F. Liu, L. Li, J. Dai and T. Liu, *Adv. Condens. Matter Phys.*, 2018, 9795654, DOI: 10.1155/2018/9795654.
53 S. David, K. Sefiane and L. Tadrist, *Colloids Surf., A*, 2007, **298**, 108–114, DOI: 10.1016/j.colsurfa.2006.12.018.

54 K. Sefiane, S. K. Wilson, S. David, G. J. Dunn and B. R. Duffy, *Phys. Fluids*, 2009, **21**, 062101, DOI: 10.1063/1.3131062.
55 Y. Xue, X. Li, H. Li and W. Zhang, *Nat. Commun.*, 2014, **5**, 4348, DOI: 10.1038/ncomms5348.
56 F. C. Marques, R. S. Alves, D. P. dos Santos and G. F. S. Andrade, *Phys. Chem. Chem. Phys.*, 2022, **24**, 27449–27458, DOI: 10.1039/D2CP04052G.
57 A. de Barros, F. M. Shimizu, C. S. de Oliveira, F. A. Sigoli, D. P. dos Santos and I. O. Mazali, *ACS Appl. Nano Mater.*, 2020, **3**, 8138–8147, DOI: 10.1021/acsanm.0c01741.
58 T.-S. Wong, T.-H. Chen, X. Shen and C.-M. Ho, *Anal. Chem.*, 2011, **83**, 1871–1873, DOI: 10.1021/ac102963x.
59 H. Y. Erbil and R. A. Meric, *J. Phys. Chem. B*, 1997, **101**(35), 6867–6873, DOI: 10.1021/jp970328n.
60 H. Y. Erbil, G. McHale, S. M. Rowan and M. I. Newton, *J. Adhes. Sci. Technol.*, 1999, **13**(12), 1375–1391, DOI: 10.1163/156856199X00532.
61 J. A. Ahumada-Lazo and R.-H. Chen, *Int. J. Therm. Sci.*, 2022, **178**, 107582, DOI: 10.1016/j.ijthermalsci.2022.107582.
62 L. Bansal, P. Seth, B. Murugappan and S. Basu, *Appl. Phys. Lett.*, 2018, **112**, 211605, DOI: 10.1063/1.5026938.
63 M. L. Bender and M. C. Neveu, *J. Am. Chem. Soc.*, 1958, **20**, 5388–5391, DOI: 10.1021/ja01552a056.
64 K. Ishizu, M. Nunomura and T. Fukutomi, *J. Polym. Sci., Part A:Polym. Chem.*, 1987, **25**, 1163–1175, DOI: 10.1002/pol.1987.170250503.
65 P. I. Nagy, *Int. J. Mol. Sci.*, 2014, **15**, 19562–19633, DOI: 10.3390/ijms151019562.
66 J. Wang, K. Zheng, B. Lin and Y. Weng, *RSC Adv.*, 2017, **7**, 34783–34794, DOI: 10.1039/C7RA06263F.
67 D. M. Tschaen, E. Turos and S. M. Weinreb, *J. Org. Chem.*, 1984, **49**, 5058–5064, DOI: 10.1021/jo00200a006.
68 K. P. Reber, S. D. Tilley and E. J. Sorensen, *Chem. Soc. Rev.*, 2009, **38**, 3022–3034, DOI: 10.1039/B901614J.
69 K. S. Nalivela, M. Rudolph, E. S. Baeissa, B. G. Alhogbi, I. A. I. Mkhalid and A. S. K. Hashmi, *Adv. Synth. Catal.*, 2018, **360**, 2183–2190, DOI: 10.1002/adsc.201800201.
70 D. Gentili and G. Ori, *Nanoscale*, 2022, **14**, 14385–14432, DOI: 10.1039/D2NR02640F.
71 S. Pal, A. Dutta, M. Paul and A. Chattopadhyay, *J. Phys. Chem. C*, 2020, **124**, 3204–3210, DOI: 10.1021/acs.jpcc.9b10689.
72 Y.-F. Huang, D.-Y. Wu, H.-P. Zhu, L.-B. Zhao, G.-K. Liu, B. Ren and Z.-Q. Tian, *Phys. Chem. Chem. Phys.*, 2012, **14**, 8485–8497, DOI: 10.1039/C2CP40751A.
73 E. B. Secor, D. Yeboah and L. Gamba, *Nanoscale*, 2025, **17**, 18997–19020, DOI: 10.1039/D5NR02110C.
74 B. Molleman and T. Hiemstra, *Environ. Sci.: Nano*, 2017, **4**, 1314–1327, DOI: 10.1039/C6EN00564K.
75 V. Ow, Q. Lin, J. H. M. Wong, B. Sim, Y. L. Tan, Y. Leow, R. Goh and X. J. Loh, *Nanoscale*, 2025, **17**, 6960–6980, DOI: 10.1039/D4NR03706E.
76 Z. Shen, W. Baker, H. Ye and Y. Li, *Nanoscale*, 2019, **11**, 6108–6117, DOI: 10.1039/C8NR09617A.
77 H. Gelderblom, C. Diddens and A. Marin, *Soft Matter*, 2022, **18**, 8535–8553, DOI: 10.1039/D2SM00931E.
78 A. T. Hoang, L. Hu, A. K. Katiyar and J.-H. Ahn, *Matter*, 2022, **5**, 4116–4132, DOI: 10.1016/j.matt.2022.08.019.
79 A. A. Balandin, F. Kargar, T. T. Salguero and R. K. Lake, *Mater. Today*, 2022, **55**, 74–91, DOI: 10.1016/j.mattod.2022.03.010.
80 X. Mei, T. Hu, Y. Wang, X. Weng, R. Liang and M. Wei, *Wiley Interdiscip. Rev.:Nanomed. Nanobiotechnol.*, 2020, **12**, e1596, DOI: 10.1002/wnan.1596.
81 Y. Zhang, J. Liu, C. Rong, D. Wang, W. Li, Z. Gao and Y. Chen, *Langmuir*, 2024, **40**, 18821–18836, DOI: 10.1021/acs.langmuir.4c01725.
82 N. Rohaizad, C. C. Mayorga-Martinez, M. Fojtů, N. M. Latiff and M. Pumera, *Chem. Soc. Rev.*, 2021, **50**, 619–657, DOI: 10.1039/D0CS00806B.
83 S. Zhang, T. Yu, H. Wen, Z. Ni, Y. He, R. Guo, J. You and X. Liu, *Chem. Commun.*, 2020, **56**, 15387–15405, DOI: 10.1039/D0CC05876A.
84 U. Dey and A. Chattopadhyay, *J. Mater. Chem. C*, 2024, **12**, 5506–5516, DOI: 10.1039/D3TC04768K.
85 L. Wang, S. Yin, J. Yang and S. X. Dou, *Small*, 2023, **19**, 2300165, DOI: 10.1002/smll.202300165.
86 U. Dey and A. Chattopadhyay, *Adv. Quantum Technol.*, 2025, **8**, 2400569, DOI: 10.1002/qute.202400569.
87 B. A. Kolesov, *Int. J. Mol. Sci.*, 2021, **22**, 5380, DOI: 10.3390/ijms22105380.
88 A. A. Zavitsas, *Spectrochim. Acta, Part A*, 2015, **151**, 553–565, DOI: 10.1016/j.saa.2015.06.079.

